Transient x-ray diffraction with simultaneous imaging under high strain-rate loading

D. Fan,[1] L. Lu,[1,2] B. Li,[1,2] M. L. Qi,[3] J. C. E,[1] F. Zhao,[1] T. Sun,[4] K. Fezzaa,[4] W. Chen,[5] and S. N. Luo[1,a)]

[1]*The Peac Institute of Multiscale Sciences, Chengdu, Sichuan 610207, People's Republic of China*
[2]*Department of Modern Mechanics, University of Science and Technology of China, Hefei, Anhui 230027, People's Republic of China*
[3]*School of Science, Wuhan University of Technology, Wuhan, Hubei 430070, People's Republic of China*
[4]*Advanced Photon Source, Argonne National Laboratory, Argonne, Illinois 60439, USA*
[5]*School of Aeronautics and Astronautics, and School of Material Science Engineering, Purdue University, West Lafayette, Indiana 47907, USA*

(Received 8 September 2014; accepted 21 October 2014; published online 7 November 2014)

Real time, *in situ*, multiframe, diffraction, and imaging measurements on bulk samples under high and ultrahigh strain-rate loading are highly desirable for micro- and mesoscale sciences. We present an experimental demonstration of multiframe transient x-ray diffraction (TXD) along with simultaneous imaging under high strain-rate loading at the Advanced Photon Source beamline 32ID. The feasibility study utilizes high strain-rate Hopkinson bar loading on a Mg alloy. The exposure time in TXD is 2–3 μs, and the frame interval is 26.7–62.5 μs. Various dynamic deformation mechanisms are revealed by TXD, including lattice expansion or compression, crystal plasticity, grain or lattice rotation, and likely grain refinement, as well as considerable anisotropy in deformation. Dynamic strain fields are mapped via x-ray digital image correlation, and are consistent with the diffraction measurements and loading histories. © *2014 AIP Publishing LLC*. [http://dx.doi.org/10.1063/1.4900861]

I. INTRODUCTION

Dynamic material response under high (10^2–10^5 s^{-1}) and ultrahigh (10^5–10^{10} s^{-1}) strain-rate loading is heavily dependent on loading rate and path, and microstructure.[1–6] Characterizing structure-property relations, revealing novel phenomena and underlying mechanisms, and developing physics-based, predictive models all require *in situ*, real time, temporally and spatially resolved measurements.

X-ray diffraction is desirable for characterizing microstructure such as grain orientation, unit cell shape, and deformation.[7,8] For example, x-ray diffraction was used to reveal microstructure and deformation mechanisms,[9] but these experiments are under quasistatic conditions. In previous dynamic experiments at synchrotrons including the Advanced Photon Source (APS), ultrafast and high-speed x-ray diffraction, and imaging measurements on bulk samples under Hopkinson bar and gas gun loading were demonstrated.[10–14] However, diffraction and imaging measurements were not done simultaneously.

While one has witnessed significant progresses in dynamic diffraction with synchrotron x-rays,[10,13,14] including ultrafast (single pulse, ~100 ps) x-ray diffraction, obtaining shock "movies" of two-dimensional (2D) diffraction patterns is still a challenge. A key reason is that the scattered x-rays contributing to diffraction signals are much weaker than the transmitted x-rays forming images. Detectors, in particular, high quantum efficiency high speed cameras, are a bottleneck in scattering measurements, and improving detection is inevitable for obtaining "diffraction movies."

As an optical technique, digital image correlation (DIC) plays an important role in estimating full-field deformation.[15–17] We recently developed an x-ray digital image correlation (XDIC) technique, which can be used for high-speed strain field mapping under dynamic loading.[18] The lattice deformation information important for understanding deformation mechanisms cannot be revealed by XDIC, though. Thus, it is also highly desirable to combine dynamic XDIC and transient x-ray diffraction (TXD) for simultaneous, multiscale measurements.

In this work, we implement a scheme to improve multiframe TXD measurements by combining an external microchannel plate (MCP) and a low-cost CMOS high-speed camera, along with simultaneous imaging measurements. We demonstrate this methodology with high strain-rate Hopkinson bar loading of an Mg alloy. These measurements reveal dynamic deformation mechanisms at micro- and mesoscales, including strain concentration, shear damage, and anisotropic deformation at lattice and grain levels. Section II addresses the experimental details and data analysis, and Sec. III presents results and discussion, followed by conclusions in Sec. IV.

II. METHODOLOGY

The experimental setup is shown in Fig. 1 for simultaneous, multiframe, TXD, and imaging measurements under high strain-rate loading. Additional information on the gas gun and Hopkinson bar systems, dynamic experiment procedure, detection, system integration, and synchronization was presented in Refs. 10 and 11.

a)sluo@pims.ac.cn

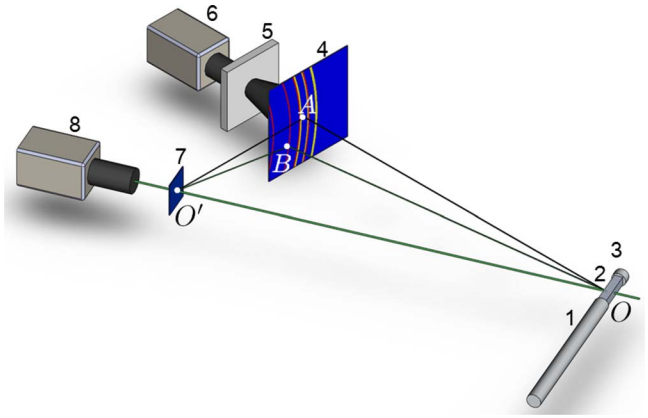

FIG. 1. Schematic of experimental setup for simultaneous transient x-ray diffraction and imaging under high strain rate loading. (1) Hopkinson bar; (2) sample; (3) force transducer; (4) diffraction scintillator (with illustrative diffraction rings); (5) microchannel plate (MCP); (6) high-speed camera for diffraction; (7) imaging scintillator; (8) high speed camera for imaging; OO': transmitted x-ray beam.

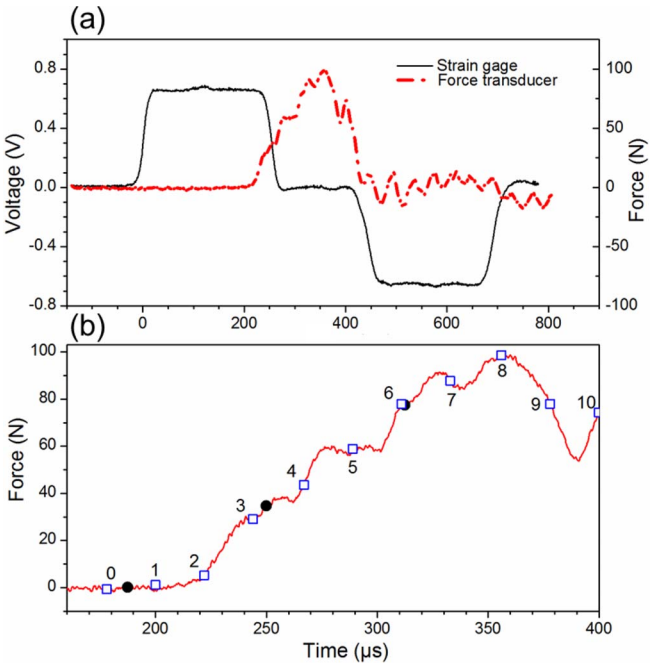

FIG. 2. (a) Strain gage and force transducer signals acquired for sample #AZ31-17 under Hopkinson tension bar loading. (b) The force transducer signal showing the instants for the snapshots of imaging (t_0–t_{10}; squares noted with numbers 0–10) and of diffraction (filled circles).

A loading device ("1" in Fig. 1), either a gas gun or split Hopkinson pressure/tension bar, dynamically loads a sample ("2") under consideration at high or ultrahigh strain rates, ranging from 10^2 s^{-1} to 10^7 s^{-1}. In current experiments, we use a Hopkinson tension bar loading system without the transmission bar, due to space limitations in the experimental hutch of the APS beamline 32ID-B. (A complete Hopkinson bar system with a smaller bar diameter will be installed at 32ID-B for future experiments.) Instead, a force transducer ("3"), i.e., a Kistler low impedance fast response quartz load cell, is used to record the force history; the strain gage located on the incident bar supplies the trigger to high-speed cameras and oscilloscopes (Fig. 2). The incident bar and striker, 12.7 mm in diameter, are made of high-strength steel.

The probe x-rays are from an APS "undulator A" light source,[10] and the energy spectra for different undulator gaps are shown in Fig. 3. In addition, we place a 1-mm thick (100) Si single crystal in the upstream path of the sample to filter x-rays, in order to reduce the heat load on the sample and other objects downstream. The spectra with filtration by the Si crystal and the sample itself are used for indexing diffraction peaks. We use this "white beam" for diffraction and imaging, i.e., the lowest harmonics (e.g., 1st–4th) presumably all contribute to diffraction and image signals. The x-ray spot on the sample is about 1 mm × 1 mm.

The incident x-rays transmitted through the sample are incident on the imaging scintillator $Lu_3Al_5O_{12}$:Ce or LuAG:Ce ("7" in Fig. 1), and the scattered x-rays, on the diffraction scintillator $Lu_{2-2x}Y_{2x}SiO_5$:Ce or LYSO:Ce ("4"). The LuAG scintillator is 100 μm thick, while the LYSO scintillator is 300 μm thick. Lenses are placed after the diffraction scintillator to increase the effective q-range (q: momentum transfer). Remapping of a diffraction "image" back to the scintillator is considered in data analysis. An MCP ("5", Quantum Leap E, Stanford Computer Optics, Inc.) is placed behind the lenses to intensify the optical signals converted from the scattered x-rays. The MCP unit is synchronized with the camera for diffraction during experiment. The recording camera for imaging is Photron Fastcam SA1.1 ("8") and that for diffraction is Photron Fastcam SA4 ("6"). Both of them use 12-bit CMOS sensors. The full frame capabilities of this imaging system have 1024 × 1024 pixels, and the pixel size is 20 μm. Their global electronic shutters can operate at 1 μs, independent of frame rate, while the number of activated pixels or the effective field of view decreases with increasing frame rates. In this work, the exposure time in TXD is 2–3 μs, and the frame interval is 26.7–62.5 μs. The exposure time for imaging is 1 μs, and the frame intervals are 22.2 μs.

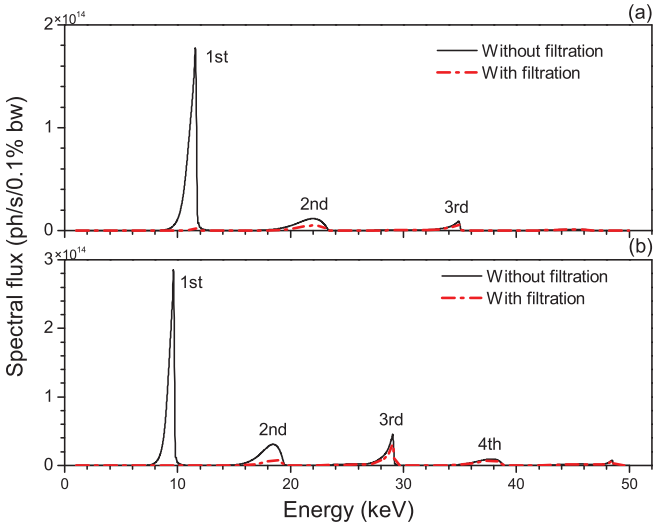

FIG. 3. Spectral flux for APS undulator-A x-ray source with a gap of 25 mm (a) and 21 mm (b). The dashed lines represent filtration by a 1-mm thick Si (100) filter and the Mg alloy sample itself. The harmonic numbers (1st–4th) are marked.

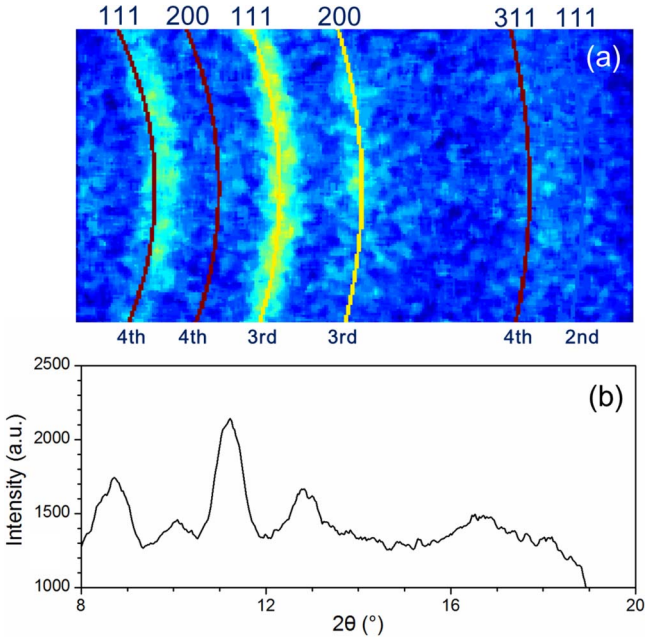

FIG. 4. (a) 2D diffraction pattern of an Al foil under ambient conditions, and (b) the integrated 1D diffraction pattern. In (a), the (*hkl*) planes (top) and the corresponding x-ray harmonics (bottom) are marked.

In Fig. 1, O and O' denote the incident points on the sample and on the imaging scintillator, respectively. OA is the normal of the diffraction scintillator, and $O'A$ is on the plane of this scintillator. For a given setup, the positions of O, O', and A ("anchor points") establish the coordinate system, and need to be determined accurately for indexing diffraction spots. The positions of the anchor points are first measured with rulers. To obtain their exact coordinates and also to calibrate the scattering angle θ for diffraction analysis, we place an Al foil in the sample position and record the diffraction patterns. The camera runs at a low speed mode so the effective field of view or q-range is larger than at a high-speed mode during dynamic loading. We choose Al for its high symmetry with relatively simple diffraction patterns. The polycrystalline Al foil yields multiple highly diffuse diffraction rings (Fig. 4).

For a diffraction spot B on the diffraction scintillator, the scattering angle θ satisfies $2\theta = \angle O'OB$. For given (*hkl*) planes, the interplanar or d-spacing is

$$d_{hkl} = \frac{\lambda}{2\sin\theta}, \tag{1}$$

where λ is the wavelength of x-rays. The strain associated with such planes is thus

$$\varepsilon_{hkl} = \frac{d_{hkl} - d_{0,hkl}}{d_{0,hkl}}. \tag{2}$$

Here subscript 0 denotes a reference configuration.

To index the diffraction rings, we fine-tune the positions of the anchor points during simulation until the simulated diffraction rings best fit the data. For the case shown in Fig. 4, the diffraction rings are from the 3rd and 4th harmonics, with a faint (111) ring from the 2nd harmonic. The diffraction rings are integrated azimuthally into 1D diffraction pattern (intensity vs. 2θ) for camera calibration. If the camera is moved further away from O' (larger 2θ), the diffraction rings can be recorded from the 1st harmonic. This, along with the undulator gap adjusting, gives one freedom to choose certain harmonics for diffraction. With the anchor points determined and the camera calibrated, we proceed to perform dynamic experiments with simultaneous diffraction and imaging.

Given an image sequence, the displacement field maps at different time, $\mathbf{u}(x, y)$, can be obtained via XDIC analysis,[18] from which strain field maps are calculated. Let $\mathbf{x}$ be the position vector and $\mathbf{u}$ be the displacement vector in the material coordinate system. The Green-Lagrangian strain tensor is defined as

$$\mathbf{E} = \frac{1}{2}\left[(\nabla_{\mathbf{x}}\mathbf{u})^T + \nabla_{\mathbf{x}}\mathbf{u} + (\nabla_{\mathbf{x}}\mathbf{u})^T \cdot (\nabla_{\mathbf{x}}\mathbf{u})\right]. \tag{3}$$

Then, the von Mises equivalent strain tensor follows as

$$E_{\text{eq}} = \sqrt{\frac{2}{3}\mathbf{E}^{\text{dev}} : \mathbf{E}^{\text{dev}}}, \tag{4}$$

where the deviatoric strain tensor is

$$\mathbf{E}^{\text{dev}} = \mathbf{E} - \frac{1}{3}\text{tr}(\mathbf{E})\mathbf{I}. \tag{5}$$

Here $\mathbf{I}$ is the unit tensor. The strain field map at t_i is obtained via image correlation of the image at t_i with that at t_{i-1}.

III. RESULTS AND DISCUSSION

To demonstrate the feasibility of multiframe TXD with simultaneous imaging, we perform Hopkinson tension bar loading on Mg alloy AZ31. The matrix of AZ31 is composed of hexagonal close-packed Mg, and the second phase is β-phase (body-centered cubic) $Al_{12}Mg_{17}$. The second phase has a particle size of 10–50 μm, and is dispersed in the Mg matrix, giving rise to the speckle pattern in the x-ray images. The sample gage length is 2 mm, the lateral dimension is 1.5 mm, and the thickness along the x-ray beam is 0.5 mm. Two samples are tested under dynamic tension; the strain gage signals on the incident bar and force histories are presented in Figs. 2 and 5, and imaging and diffraction results, in Figs. 6–9.

The strain gage signals of the incident and reflected pulses are of similar amplitudes, largely owing to the impedance mismatch between the sample and the incident bar. Only the incident pulse signals are shown in Figs. 2 and 5. The force histories show approximately two segments t_1–t_4 and t_6–t_8 on the rise in Fig. 2(b) for sample #AZ31-17, and t_0–t_3 and t_3–t_5 on the rise in Fig. 5 for sample #AZ31-10. However, the elastic–plastic transitions are not definitive. The rapid drop right after the peak stress (force) is due to tensile failure. Measurements exhibiting similar deformation and failure features were obtained previously.[19–22]

The strain maps $E_{\text{eq}}(x, y)$ for sample #AZ31-17 exhibit four stages of deformation (Fig. 6): elastic deformation (t_1–t_2), "inhomogeneous" plastic deformation (t_3–t_5), homogenization of plastic deformation (t_6–t_8), and shear failure (t_9–t_{10}). The deformation during t_3–t_5 show two distinct regions (left and right) with different degrees of deformation, likely due to two different grains. The deformation becomes homogenized during t_6–t_8 as deformation proceeds. These maps are consistent with, although not exact the same as, the

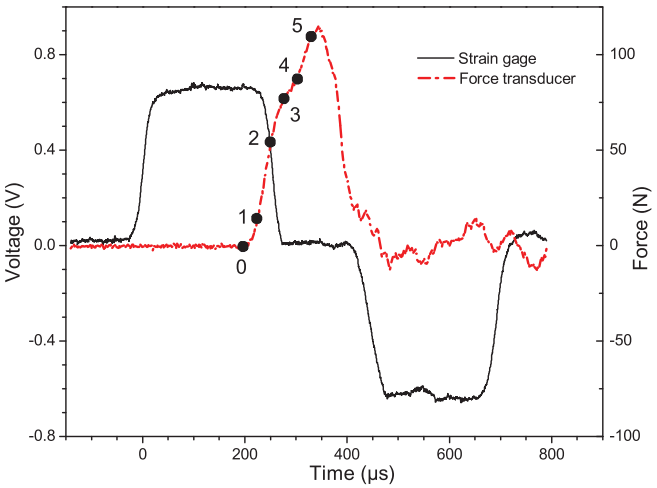

FIG. 5. Strain gage and force transducer signals acquired for sample #AZ31-10 under Hopkinson tension bar loading. The instants for diffraction snapshots (t_0–t_5; marked as numbers 0–5) are also shown on the force transducer curve. The frame separation is 26.7 μs.

force histories, since the latter lack sufficient "resolution" to distinguish minor elastic deformation, inhomogeneous plastic deformation and its homogenization on the rise. During failure, the shear failure (t_9–t_{10}) as identified from the strain fields coincides with the force histories. Thus, distinguishing deformation modes simply from the shape of a stress–strain or loading curve might be crude in some cases.

The 2D diffraction patterns (Fig. 7) are measured on sample #AZ31-17 simultaneously with imaging (Fig. 6), but at a slower framing rate in order to achieve a larger q-range. These two measurements are consistent. Figure 7(a) shows the diffraction pattern before the loading pulse arrives (187.5 μs, between t_0 and t_1 in Figs. 2 and 6). The main diffraction spots are indexed as (100), (002), (110), and (103) from the 2nd and 3rd harmonics. The upper and lower (100) spots are from two different grains. During dynamic tension (250 μs, between t_3 and t_4), both the upper and lower (100) spots move left toward smaller 2θ. For the lower (100) spot, d_{100} increases by 0.154 Å or 5.6%, and the full-width at half maximum (FWHM), by ~3% (Fig. 8). The upper (100) spot shows much more pronounced broadening along both the 2θ and azimuthal directions, as well as increase in the d-spacing, than the lower (100) spot. This is highly likely caused by different deformation in different grains, as indicated by the strain map snapshots t_3 and t_4 (Fig. 6). At a time frame (312.5 μs, t_6), both (100) spots move out of the field of view likely due to accumulated lattice extension. The diffraction patterns are consistent with the strain maps and the loading history.

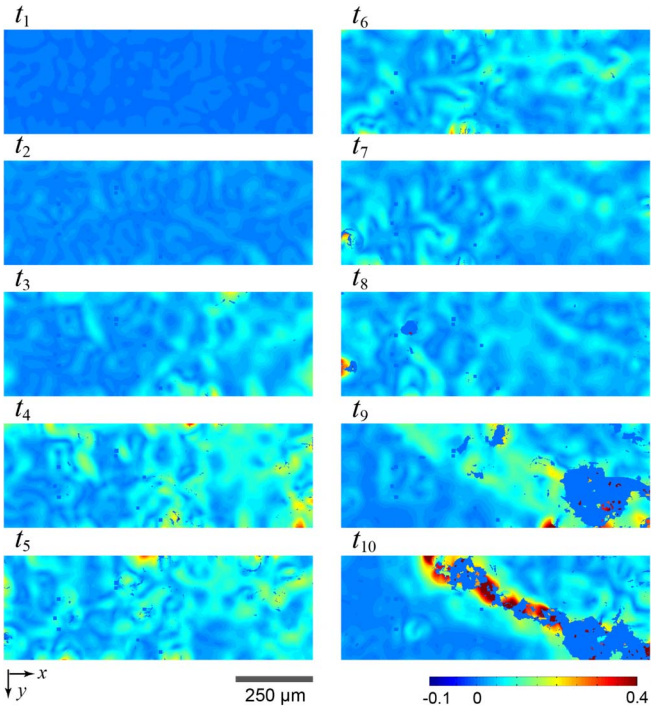

FIG. 6. Sequence of von Mises equivalent strain $E_{eq}(x, y)$ maps obtained from XDIC analysis of image sequence t_0–t_{10} (also refer to Fig. 2). The frame interval is 22.2 μs.

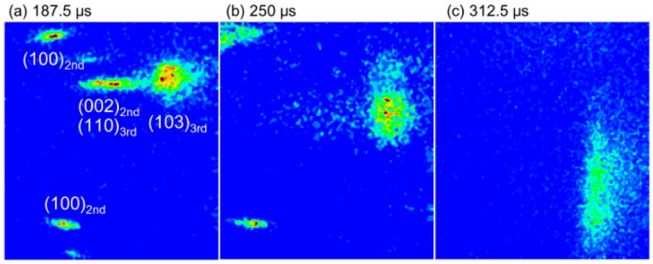

FIG. 7. Snapshots of 2D diffraction patterns of sample #AZ31-17 under Hopkinson tension bar loading. The frame interval is 62.5 μs. The subscripts denote the harmonic numbers in Fig. 3(a). Also refer to Fig. 2 for the corresponding loads. The undulator gap is 25 mm. (a) 187.5 μs. (b) 250 μs. (c) 312.5 μs.

The diffraction patterns for sample #AZ31-17 (Fig. 7) reveal features that can be attributed to lattice expansion, plasticity, grain, or lattice rotation (changes in the azimuthal angle), and likely grain refinement, and show considerable anisotropy in deformation. One example is the changes in the

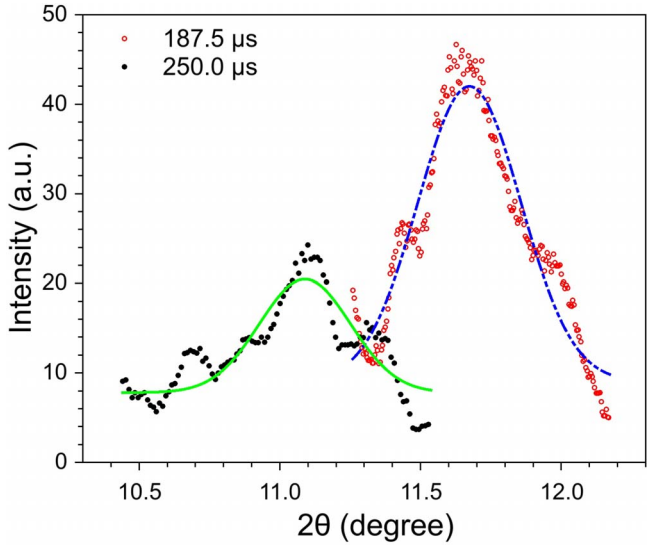

FIG. 8. Shift and broadening of the (100) diffraction spot (the lower one in Fig. 7) due to dynamic tension.

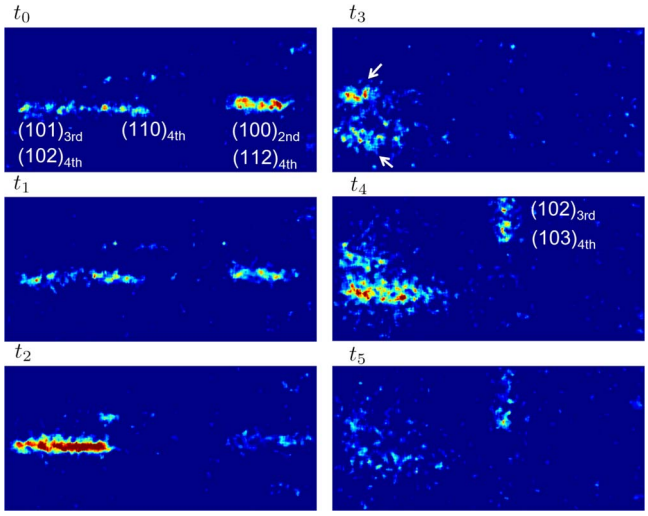

FIG. 9. Snapshots of 2D diffraction patterns of sample #AZ31-10 under Hopkinson tension bar loading. The frame separation is 26.7 μs, and the q-range is thus smaller than that for sample #AZ31-10 in Fig. 7. Also refer to Fig. 5 for timing. The undulator gap is 21 mm.

two (100) spots related to two grains with different orientations as discussed above. The (110) and (002) spots undergo a small clockwise rotation and then become highly diffuse. The (103) spot rotates clockwise by about 3.3° and broadened appreciably azimuthally (Fig. 7(b)). The interplanar spacing experiences little expansion, i.e., $\Delta d_{103} \sim 0$ even under a large accumulated strain at 312.5 μs (t_6 in Fig. 6).

For sample #AZ31-10, the diffraction patterns (Fig. 9) are also consistent with the loading curve (Fig. 5), similar to sample #AZ31-17. Plastic deformation occurs at t_2–t_3 as indicated by the smearing of (100) and (112) spots. Interestingly, the $(101)_{3rd}$ and $(102)_{4th}$ spots become sharper and intenser, and a possible reason is stress-induced defect annihilation. The plastic regime on the loading curve (t_3–t_5) is with pronounced lattice deformation, including splitting of $(101)_{3rd}$ and $(102)_{4th}$ spots at t_3 (indicated by two arrows, Fig. 9), and subsequent smearing, as well as lattice rotation. The splitting is likely caused by twinning or formation of a new grain. The entrance of $(102)_{3rd}$ and $(103)_{4th}$ from the top into the field of view is induced by grain rotation.

Dynamic multiframe diffraction measurements can be extended into the reflection mode for x-ray opaque samples, although simultaneous imaging is not doable in such cases. The external MCP does improve the signal-to-noise ratio recorded by the low-cost high-speed camera for diffraction, but the camera frame rate and effective field of view are still unsatisfactory. The x-ray spot size/sampling volume need to be considered as regards microstructure for diffraction measurement and interpretation. Optimizing the undulator x-ray source spectra, such as reducing the bandwidth of high harmonics, is useful for improving q-resolution.

IV. CONCLUSIONS

We present an experimental demonstration of multiframe transient x-ray diffraction along with simultaneous imaging (dynamic strain field mapping) under high strain-rate loading. High strain-rate Hopkinson bar loading on a Mg alloy is used for the feasibility study. TXD is done in the transmission mode, while it can be extended into the reflection mode; the exposure time is 2–3 μs, and the frame interval is 26.7–62.5 μs, as limited by current high-speed cameras. The diffraction patterns reveal dynamic deformation mechanisms including lattice expansion or compression, crystal plasticity, grain or lattice rotation, and likely grain refinement, as well as considerable anisotropy in deformation. Dynamic strain-field mapping and loading histories are consistent with the diffraction measurements, demonstrating the potential of the current technique in the micro- and mesoscale studies.

ACKNOWLEDGMENTS

We would like to thank M. Hudspeth, N. Parab, Z. Guo, A. Deriy, and J. Wang for their various help. Use of the Advanced Photon Source and the Center for Nanoscale Materials were supported by the U.S. Department of Energy, Office of Science, Office of Basic Energy Sciences, under Contract No. DE-AC02-06CH11357. This work was supported in part by the National Natural Science Foundation of China and NSAF (Nos. 11472253, 11172221, and U1330111).

[1]L. Davison and R. A. Graham, Phys. Rep. **55**, 255 (1979).
[2]P. Follansbee and C. Frantz, J. Eng. Mater. Technol. **105**, 61 (1983).
[3]M. A. Meyers, *Dynamic Behavior of Materials* (Wiley, New York, 1994).
[4]Q. Wei, T. Jiao, K. Ramesh, and E. Ma, Scripta Mater. **50**, 359 (2004).
[5]R. Chen, K. Xia, F. Dai, F. Lu, and S. N. Luo, Eng. Fract. Mech. **76**, 1268 (2009).
[6]G. I. Kanel, Int. J. Fract. **163**, 173 (2010).
[7]B. Jakobsen, H. F. Poulsen, U. Lienert, J. Almer, S. D. Shastri, H. O. Sørensen, C. Gundlach, and W. Pantleon, Science **312**, 889 (2006).
[8]R. Barabash, G. Ice, and F. Walker, J. Appl. Phys. **93**, 1457 (2003).
[9]S. Van Petegem, J. Zimmermann, and H. Van Swygenhoven, Acta Mater. **61**, 5846 (2013).
[10]S. N. Luo, B. J. Jensen, D. E. Hooks, K. Fezzaa, K. J. Ramos, J. D. Yeager, K. Kwiatkowski, and T. Shimada, Rev. Sci. Instrum. **83**, 073903 (2012).
[11]M. Hudspeth, B. Claus, S. Dubelman, J. Black, A. Mondal, N. Parab, C. Funnell, F. Hai, M. L. Qi, K. Fezzaa, S. N. Luo, and W. Chen, Rev. Sci. Instrum. **84**, 025102 (2013).
[12]W. W. Chen, M. C. Hudspeth, B. Claus, N. D. Parab, J. T. Black, K. Fezzaa, and S. N. Luo, Philos. Trans. R. Soc. A **372**, 20130191 (2014).
[13]S. J. Turneaure, Y. M. Gupta, K. Zimmerman, K. Perkins, C. S. Yoo, and G. Shen, J. Appl. Phys. **105**, 053520 (2009).
[14]P. K. Lambert, C. J. Hustedt, K. S. Vecchio, E. L. Huskins, D. T. Casem, S. M. Gruner, M. W. Tate, H. T. Philipp, A. R. Woll, P. Purohit, J. T. Weiss, V. Kannan, K. T. Ramesh, P. Kenesei, J. S. Okasinski, J. Almer, M. Zhao, A. G. Ananiadis, and T. C. Hufnagel, Rev. Sci. Instrum. **85**, 093901 (2014).
[15]T. C. Chu, W. F. Ranson, and M. A. Sutton, Exp. Mech. **25**, 232 (1985).
[16]H. A. Bruck, S. R. McNeill, M. A. Sutton, and W. H. Peters III, Exp. Mech. **29**, 261 (1989).
[17]B. Pan, K. Qian, H. Xie, and A. Asundi, Meas. Sci. Technol. **20**, 062001 (2009).
[18]L. Lu, D. Fan, B. X. Bie, X. X. Ran, M. L. Qi, N. Parab, J. Z. Sun, H. J. Liao, M. C. Hudspeth, B. Claus, K. Fezzaa, T. Sun, W. Chen, X. L. Gong, and S. N. Luo, Rev. Sci. Instrum. **85**, 076101 (2014).
[19]B. Li, S. Joshi, K. Azevedo, E. Ma, K. Ramesh, R. Figueiredo, and T. Langdon, Mater. Sci. Eng. A **517**, 24 (2009).
[20]G. Bajargan, G. Singh, D. Sivakumar, and U. Ramamurty, Mater. Sci. Eng. A **579**, 26 (2013).
[21]F. Kang, J. T. Wang, and Y. Peng, Mater. Sci. Eng. A **487**, 68 (2008).
[22]N. Dudamell, I. Ulacia, F. Galvez, S. Yi, J. Bohlen, D. Letzig, I. Hurtado, and M. Perez-Prado, Mater. Sci. Eng. A **532**, 528 (2012).